

When holography meets coherent diffraction imaging

Tatiana Latychevskaia*, Jean-Nicolas Longchamp and Hans-Werner Fink

Physics Institute
University of Zurich
Winterthurerstrasse 190
8057 Zurich
Switzerland

Corresponding author:
e-mail: tatiana@physik.uzh.ch

Introduction

In understanding the physical, chemical and biological properties of a molecule by obtaining detailed information about its structure, there is an ultimate wish: the visualization of this very molecule in three dimensions at atomic scale, rather than obtaining structural information by averaging over an ensemble of molecules.

Coherent diffraction imaging¹ (CDI) is a modern lens-less imaging technique promising exactly that: visualizing an individual molecule at the highest possible resolution² solely limited by the radiation wavelength. Individual bacteria and viruses have been imaged by CDI employing coherent X-rays³⁻⁵ and recently, CDI has been extended to recover the three-dimensional shape of objects from a single diffraction pattern⁶. Higher resolution is expected with the implementation of bright coherent radiation from X-ray free electron lasers⁷. Since detectors are only sensitive to intensity, i.e. the square-amplitude of the complex-valued scattered wave, the phase of the wave is missing and must somehow be recovered to reconstruct the molecule's anatomy. There are two well-known solutions to this phase problem: holography⁸ and CDI¹. Both techniques have their pros and cons. In holography, the reconstruction of the scattered complex-valued object wave is provided by a well-defined reference wave that must cover the entire detector area which often is an experimental challenge. In CDI, the phase recovery is an iterative process whose outcome is not always uniquely-defined. Furthermore, CDI requires pre-known information about the object⁹. Here, we show how holography and CDI can be merged into one superior technique; holographic coherent diffraction imaging (HCDI). HCDI is based on our discovery of a mathematical relationship between holography and CDI. Its application in turn features a unique solution to the phase problem, circumvents the oversampling condition while allowing the visualization of an individual object at highest possible resolution.

The main text

A diffraction pattern of an object contains information about the object structure at a resolution provided by the highest detectable diffraction orders. The object distribution at some plane can be characterized by a transmission function $t(x,y)$ and the distribution of the scattered wave in the far-field is given by the Fourier-transform of the object

transmission function $FT[t(x,y)]$. Let (x,y) and (X,Y) be the coordinates in the object and detector plane respectively. Since only the intensity of the scattered wave can be measured, $I(X,Y) = |FT[t(x,y)]|^2$ describes the diffraction pattern. However, to reconstruct the object structure, the entire complex-valued distribution of $FT[t(x,y)]$ must be known, and thus the phase must be recovered by some means. This inverse phase problem is known to have a unique solution for two-dimensional distributions when some a priori information about the object is available (for instance, the real part of $t(x,y)$)¹⁰⁻¹¹. A method to recover the phase information from the diffraction pattern alone was proposed in 1952 by Sayre¹². He speculated that the phase of the complex-valued scattered wave $FT[t(x,y)]$ can be retrieved if the diffraction pattern is sampled with a frequency at least twice the Nyquist frequency, often referred to as the “oversampling” condition. Oversampling in the Fourier-domain results in zero-padding in the object plane, which is experimentally realized by having the object surrounded by a region with a known transmission function (vacuum, for instance). The oversampling ratio σ is given by the number of total pixels in relation to the number of pixels with unknown values. Provided that $\sigma > 2$ in all directions, the phase problem can be solved uniquely¹³. The solution is found by employing an iterative procedure¹⁴ in which the wavefront propagation between object and detector plane is computed by a Fourier transform. The constraints of the measured intensity distribution in the detector plane and the known support in the object plane are superimposed onto the computed results of propagation and back-propagation. There are several problems associated with this method. The geometry of the experimental setup must be designed to fulfill the oversampling condition. The sample must be surrounded by a support with known transmission properties. For instance, when imaging a biological molecule, it must ideally be either levitating in vacuum or resting on a homogeneous transparent film; both situations are difficult if not impossible to realize. Moreover, the presence of noise in experimental images often leads to non-unique solutions or to the stagnation of the iterative reconstruction process at some partly reconstructed object¹⁵. False reconstructions are especially misleading when the object distribution cannot be verified by another imaging technique. In practice, results of hundreds of iterative runs are required, which are subsequently averaged or the best ones are subjectively defined as the correct reconstructions^{6,16-17}. Objects exhibiting complex-valued transmission functions are also known to be difficult to recover¹⁸. Another problem is the missing signal in the central overexposed region of the diffraction pattern. The intensity ratio between the central spot and the signal at the rim of the detector can reach values of 10^7 ; commonly used 16bit cameras are simply not capable to capture the whole intensity range. Since the higher-order signals provide the desired high-resolution, the central (low-resolution) part is usually sacrificed by being blocked. However, the missing information in the central area is required to initiate the reconstruction with a low-resolution shape of the object. This missing data are usually obtained by recording a low-resolution image by some other technique, a TEM image for example², or by recording a set of images at different exposure times^{4,17}. An intensive search for better techniques has already led to the invention of novel reconstruction algorithms¹⁹ and initiated a number of novel experimental designs²⁰⁻²². Fresnel or curved beam coherent diffraction imaging^{20,23-24} uses a slightly divergent beam leading to an inline hologram in the center of the diffraction

pattern. While this method provides a unique solution in contrast to conventional CDI, the diffraction pattern is affected even by slight sample motion and the curvature of the incident wave leads to decreased resolution.

To set the stage for the method we invented, we like to start with a quote from Bates¹¹ who wrote in 1979 in “On phase problem II”: “It is seen that availability of even inaccurate phase data can greatly simplify the computational procedure...”

Straight forward available phase information is exactly what is provided by holography. Thus, in HCDI two images are recorded: a diffraction pattern and a hologram of the same object. The hologram replaces the recorded low-resolution image in conventional CDI however with the significant benefit of having immediate phase information available.

First we show that there is a firm mathematical relationship between holography and coherent diffraction; a fact that had apparently remained uncovered over the past decades. Next, based on this relationship we shall demonstrate two experimental examples of HCDI.

The reconstruction of an object distribution $t(x,y)$ from its inline hologram $H(X,Y)$ requires a deconvolution with the impulse response of a free space propagation factor²⁵⁻²⁶. According to the convolution theorem, we obtain:

$$\text{FT}(H(X,Y)) = \text{FT}(t(x,y)) \text{FT}(\exp(ikr)) \quad (1)$$

where $\exp(ikr)$ denotes the phase factor due to the free space propagation (Supplementary Discussion). In CDI, the measured intensity in the far-field is given by:

$$I(X,Y) = \left| \text{FT}(t(x,y)) \right|^2 \quad (2)$$

Eqs.(1) and (2) demonstrate that the modulus of the Fourier transform of the hologram $\left| \text{FT}(H(X,Y)) \right|$ delivers the amplitude of the scattered object wave in the far-field $\left| \text{FT}(t(x,y)) \right|$. This feature immediately solves the problem of the usually missing information in the central spot of the diffraction pattern; it can now directly be obtained from the Fourier transform of the hologram. Furthermore, the phase of $\text{FT}(H(X,Y))$ constitutes the initial phase distribution in the iterative reconstruction. Since HCDI takes advantage of the initial phase information provided by its build-in holographic part instead of starting the iteration with a random phase as in conventional CDI, the oversampling condition becomes obsolete.

Thus, the entire reconstructed area of $N \times N$ pixels can be occupied by the object, and as a consequence, the resulting resolution of the reconstructed object is higher than in conventional oversampled CDI.

A low-resolution structure of the object distribution, including its phase shifting and absorption properties^{26,27} constitutes now the start for the iterative refinement of the phase retrieval. And it is not surprising that an iterative process that begins with a good and realistic “phase guess” is more likely to converge faster and lead to an unambiguous result compared to a process bound on no information at all but forced to start with a random guess. We shall verify this notion by experiments discussed below.

An optical setup employing laser light of 532 nm wavelength has been used. It allows recording a hologram and a diffraction pattern of the same object without significant

modification, as shown in Fig. 1: only the illuminating wavefront is converted from a parallel into a spherical one. As for the object, a knotted hair is selected due to its simple geometry. Figure 2 shows the result of using the HCDI method to recover the structure of the knotted hair from its two images, the hologram (Fig. 2b) and the diffraction pattern (Fig. 2c). The squared amplitude of the Fourier transform of the hologram, displayed in Fig. 2e, exhibits a distribution which compares well to the measured diffraction pattern shown in Fig. 2d. The low-order modulations in $|\text{FT}(H(X,Y))|$ and in the diffraction pattern are found at the same positions. The higher order diffraction peaks are absent in $|\text{FT}(H(X,Y))|$ because of experimental noise in the reference wave. A hologram can be reconstructed on its own, and the results of such reconstructions are displayed in Fig. 2e, f. The details in these hologram reconstructions are blurred and the presence of the out-of-focus twin images is apparent. The respective diffraction pattern has been reconstructed using our HCDI method (see Methods). A recognizable object distribution has already been achieved just after the first iteration; further iterations only improve the resolution of the reconstruction. The amplitude and phase distributions retrieved after 300 iterations are shown in Fig. 2g, h. Fine details of about 1 pixel in size (corresponding to 1.6 μm) can be resolved in the reconstruction displayed in Fig. 2g showing that the resolution is approaching the wavelength limit.

Another application of the HCDI method is shown in Fig. 3. This time, the object, a wing of a small fly, was selected for the sake of obtaining a structure-less diffraction pattern without distinct peaks. Again, the measured diffraction pattern and the squared amplitude of the Fourier transform of the hologram are visually identical. The amplitude and phase distributions retrieved after 300 iterations are shown in Fig. 3e, f.

Although we have demonstrated the HCDI method using light optics, it can obviously also be applied to other coherent radiation such as X-rays or electrons with an expected resolution scaling with the wavelength. The holographic acquisition scheme can be realized in X-ray diffraction experiments either by shifting the Fresnel zone plate or the object, thus placing the object into a divergent beam. In CDI employing coherent electrons, the transition from a plane to a spherical wavefront can be realized by adjusting the voltage of the focusing lens²⁸⁻²⁹. For future experiments, as the information stored in a holographic image is actually three-dimensional, the method might be extended to reconstruct the three-dimensional structure of objects from their diffraction patterns.

Acknowledgements

The authors would like to acknowledge the assistance of Conrad Escher for the sample preparation. We would also like to thank Mirna Saliba for careful reading of the manuscript. The “Forschungskredit of the University of Zurich” as well as the Swiss National Science Foundation are gratefully acknowledged for their financial support.

Methods Summary

For the first loop of the iterative phase retrieval procedure the complex-valued distribution in the detector plane is composed as follows: the amplitude is given by the square root of the measured intensity; the phase is provided by $\text{FT}(H)\exp(-ikr)$, in which the factor $\exp(-ikr)$ is defined by the object position during the hologram acquisition. In

the case of an inline hologram, this factor amounts to: $\exp((i\pi\lambda D^2)(n^2+m^2)/dS^2)$, where D is the distance between the origin of the spherical wave and the screen, d is the distance between the source and the object, S is the screen size, and (m,n) denote pixel positions. This phase distribution is used only for the first iteration. The missing central region of 18 pixels in diameter is filled with the amplitude distribution of $FT(H)$ for the first 100 iterations. A non-negative absorption constraint²⁷ and a loose support mask of about 20 pixels from the object contour are applied in the object plane.

References

- 1 Miao, J. W., Charalambous, P., Kirz, J. & Sayre, D. Extending the methodology of X-ray crystallography to allow imaging of micrometre-sized non-crystalline specimens. *Nature* **400**, 342-344 (1999).
- 2 Zuo, J. M., Vartanyants, I., Gao, M., Zhang, R. & Nagahara, L. A. Atomic resolution imaging of a carbon nanotube from diffraction intensities. *Science* **300**, 1419-1421 (2003).
- 3 Miao, J. W. *et al.* Imaging whole Escherichia coli bacteria by using single-particle x-ray diffraction. *Proc. Natl. Acad. Sci. U. S. A.* **100**, 110-112 (2003).
- 4 Shapiro, D. *et al.* Biological imaging by soft x-ray diffraction microscopy. *Proc. Natl. Acad. Sci. U. S. A.* **102**, 15343-15346 (2005).
- 5 Song, C. Y. *et al.* Quantitative imaging of single, unstained viruses with coherent X-rays. *Phys. Rev. Lett.* **101**, 158101 (2008).
- 6 Raines, K. S. *et al.* Three-dimensional structure determination from a single view. *Nature* **463**, 214-217 (2010).
- 7 Chapman, H. N. & Nugent, K. A. Coherent lensless X-ray imaging. *Nature Photon.* **4**, 833-839 (2010).
- 8 Gabor, D. A new microscopic principle. *Nature* **161**, 777-778 (1948).
- 9 Fienup, J. R. Phase retrieval algorithms - a comparison. *Appl. Optics* **21**, 2758-2769 (1982).
- 10 Bates, R. H. T. On phase problems I. *Optik* **51**, 161-170 (1978).
- 11 Bates, R. H. T. On phase problems II. *Optik* **51**, 223-234 (1978).
- 12 Sayre, D. Some implications of a theorem due to Shannon. *Acta Crystallogr.* **5**, 843-843 (1952).
- 13 Sayre, D. & Chapman, H. N. X-ray microscopy. *Acta Crystallogr. A* **51**, 237-252 (1995).
- 14 Gerchberg, R. W. & Saxton, W. O. A practical algorithm for determination of phase from image and diffraction plane pictures. *Optik* **35**, 237-246 (1972).
- 15 Fienup, J. R. & Wackerman, C. C. Phase-retrieval stagnation problems and solutions. *J. Opt. Soc. Am. A - Opt. Image Sci. Vis.* **3**, 1897-1907 (1986).
- 16 Huang, W. J., Jiang, B., Sun, R. S. & Zuo, J. M. Towards sub-A atomic resolution electron diffraction imaging of metallic nanoclusters: A simulation study of experimental parameters and reconstruction algorithms. *Ultramicroscopy* **107**, 1159-1170 (2007).
- 17 Thibault, P. & Rankenburg, I. C. Optical diffraction microscopy in a teaching laboratory. *Am. J. Phys.* **75**, 827-832 (2007).

- 18 Fienup, J. R. Reconstruction of a complex-valued object from the modulus of its Fourier-transform using a support constraint. *J. Opt. Soc. Am. A - Opt. Image Sci. Vis.* **4**, 118-123 (1987).
- 19 Marchesini, S. *et al.* X-ray image reconstruction from a diffraction pattern alone. *Phys. Rev. B* **68** (2003).
- 20 Williams, G. J. *et al.* Fresnel coherent diffractive imaging. *Phys. Rev. Lett.* **97**, 025506 (2006).
- 21 Marchesini, S. *et al.* Massively parallel X-ray holography. *Nature Photon.* **2**, 560-563 (2008).
- 22 Vine, D. J. *et al.* Ptychographic Fresnel coherent diffractive imaging. *Phys. Rev. A* **80** (2009).
- 23 Williams, G. J. *et al.* Curved beam coherent diffractive imaging. *Thin Solid Films* **515**, 5553-5556 (2007).
- 24 Williams, G. J., Quiney, H. M., Peele, A. G. & Nugent, K. A. Fresnel coherent diffractive imaging: treatment and analysis of data. *New J. Phys.* **12**, 035020 (2010).
- 25 Kreis, T. M. Frequency analysis of digital holography with reconstruction by convolution. *Opt. Eng.* **41**, 1829-1839 (2002).
- 26 Latychevskaia, T. & Fink, H.-W. Simultaneous reconstruction of phase and amplitude contrast from a single holographic record. *Opt. Express* **17**, 10697-10705 (2009).
- 27 Latychevskaia, T. & Fink, H.-W. Solution to the twin image problem in holography. *Phys. Rev. Lett.* **98**, 233901 (2007).
- 28 Steinwand, E., Longchamp, J. N. & Fink, H. W. Fabrication and characterization of low aberration micrometer-sized electron lenses. *Ultramicroscopy* **110**, 1148-1153 (2010).
- 29 Steinwand, E., Longchamp, J.-N. & Fink, H.-W. Coherent low-energy electron diffraction on individual nanometer sized objects. *Ultramicroscopy* **111**, 282-284 (2011).
- 30 Debevec, P. E. & Malik, J. Recovering high dynamic range radiance maps from photographs. *SIGGRAPH* **130** (1997).

Figures

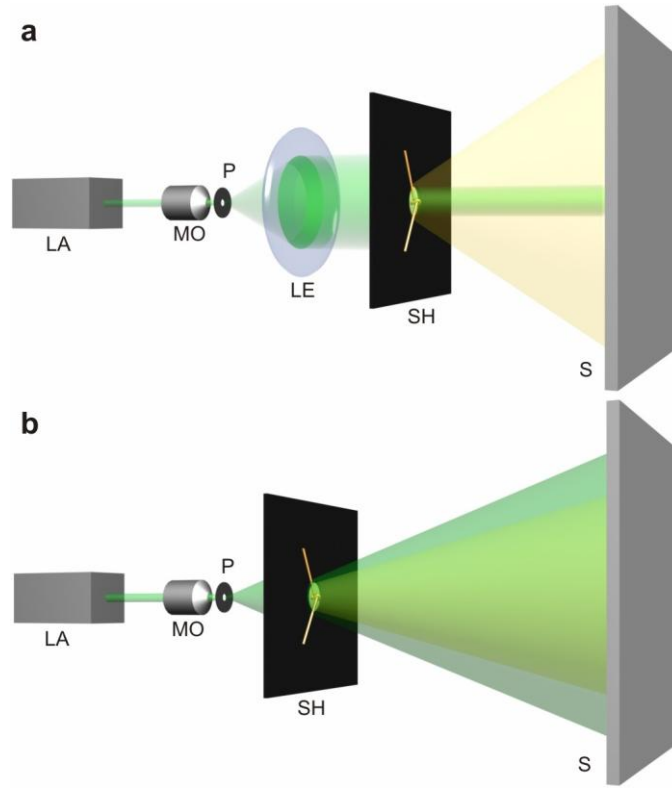


Figure 1. **Optical scheme for recording diffraction patterns and holograms.** **a**, Scheme for recording diffraction patterns. Laser light from the laser source (LA) passes the spatial filtering system (microscope objective (MO) with a NA=0.85 and pinhole (P) of diameter = 10 μm). At the sample holder (SH), the object is fixed over a 1.5 mm diameter aperture. The reconstructed object area in both modes, holography and CDI, is the same and amounts to 1.6mm. For the recording of diffraction patterns, the wavefront is broadened by a lens (LE) with $f=35$ mm, and the distance between the object and the screen is set to 905 mm. The central part of the diffraction pattern is blocked to avoid false readouts caused by the overexposure of the camera, and a set of images at different intensities is combined into one high dynamic range image³⁰. **b**, Scheme for recording holograms. The lens LE is removed and the sample is shifted closer to the pinhole P; the distance between the pinhole P and the screen is 1m. Both, diffraction patterns and holograms are recorded on a 30x30 cm² screen and sampled with 1000x1000 pixels.

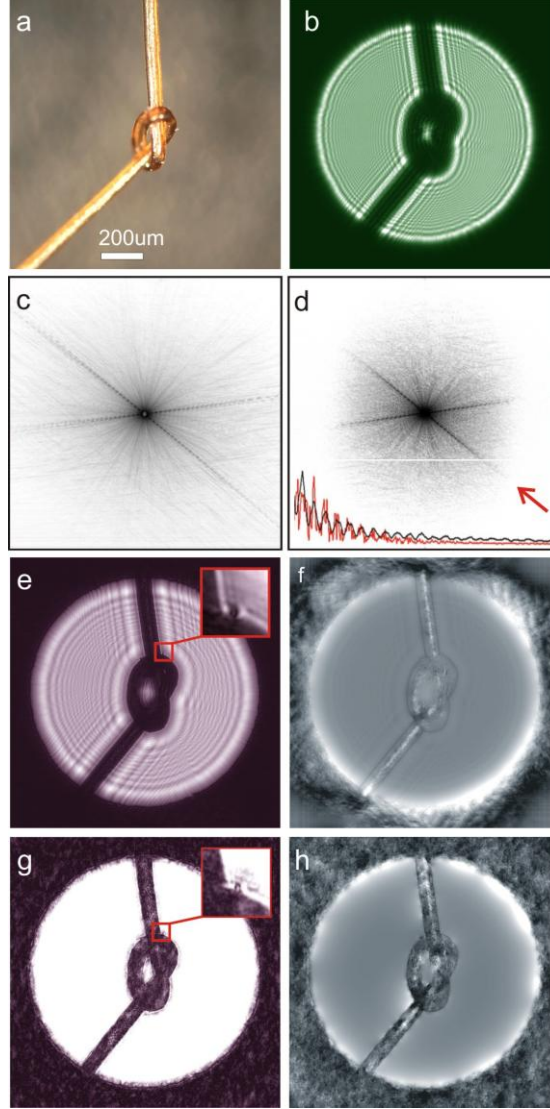


Figure 2. **HCDI reconstructions of a human hair.** **a**, Reflected-light microscopy image of a hair. **b**, Recorded hologram: the pinhole-sample distance amounts to 5.3 mm. **c**, Experimental diffraction pattern recorded at 1 m from the sample. **d**, Amplitude of the Fourier transform of the hologram. The inset shows the profiles of the square root of the experimental diffraction pattern intensity (black) and the amplitude of $FT(H)$ (red) along the direction indicated by a red arrow. The resolution provided in a hologram can be estimated by examining the amplitude of $FT(H)$, and it is usually less than the resolution provided in the diffraction pattern. **e**, Amplitude distribution reconstructed from the hologram. The superimposed interference pattern arises from the twin image. In the inset, a magnified 40x40 pixels part of the reconstruction is shown. **f**, Unwrapped phase distribution reconstructed from hologram. **g**, Amplitude distribution reconstructed with HCDI. The inset shows a magnified 40x40 pixels part of the reconstruction, demonstrating an improved resolution when comparing to the hologram reconstruction. **h**, Phase distribution reconstructed with HCDI and unwrapped.

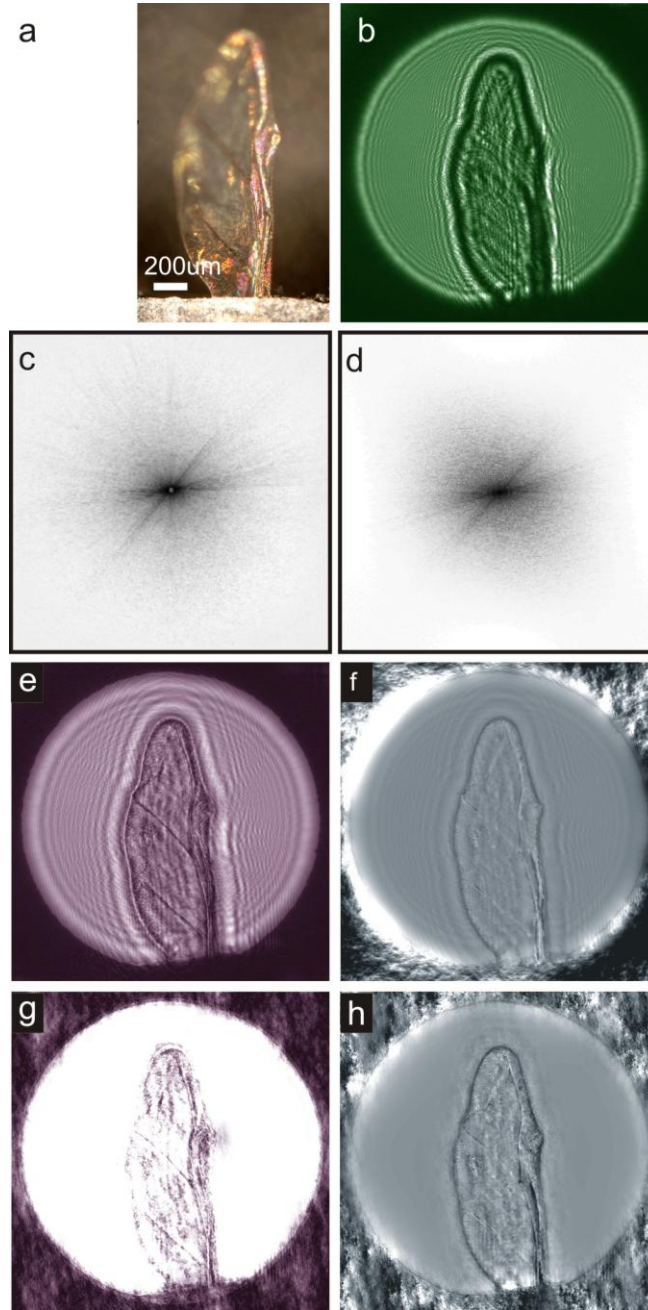


Figure 3. **HCDI reconstructions of a fly wing.** **a**, Reflected-light microscopy image of a small fly wing. **b**, Recorded hologram: the pinhole-sample distance amounts to 5.3 mm. **c**, Experimental diffraction pattern recorded at 1 m from the sample. **d**, Amplitude of the Fourier transform of the hologram. **e**, Amplitude distribution reconstructed from the hologram. **f**, Reconstructed and unwrapped phase distribution from the hologram. **g**, Amplitude distribution reconstructed with HCDI. **h**, Phase distribution reconstructed with HCDI and unwrapped.

Supplementary information

I. Reconstruction of a hologram by deconvolution

The transmission function in the object plane can be written as:

$$t(x,y) = 1 + o(x,y) = \exp(-a(x,y)) \exp(-i\phi(x,y)) \quad (\text{S1})$$

where $a(x,y)$ and $\phi(x,y)$ describe absorbing and phase shifting properties in some plane in the object domain. A incident spherical wave passing the object is described by $(1/z_0)\exp(i\pi/\lambda z_0(x^2+y^2))$, where z_0 is the distance between the origin of the wave and the object. The scattered wave in the detector plane is represented as:

$$U(X,Y) = -\frac{i}{\lambda z_0 z_s} \iint t(x,y) \exp\left(\frac{i\pi}{\lambda z_0}(x^2+y^2)\right) \exp\left(\frac{i\pi}{\lambda z_s}((x-X)^2+(y-Y)^2)\right) dx dy \quad (\text{S2})$$

Here, z_s is the distance between object and detector, and (X,Y) denote coordinates in the detector plane. The intensity in the detector plane, and thus the hologram distribution, is given by:

$$H(X,Y) = |U(X,Y)|^2 = \frac{1}{(\lambda z_0 z_s)^2} \left| \iint t(x,y) \exp\left(\frac{i\pi}{\lambda z_0} \left(\left(x - X \frac{z_0}{z_s}\right)^2 + \left(y - Y \frac{z_0}{z_s}\right)^2 \right) \right) dx dy \right|^2. \quad (\text{S3})$$

The expression under the integral can be represented as a convolution and leads to the following expression after hologram normalization (division by the intensity of the wave at the detector in the absence of the object):

$$H(X,Y) = |t(X,Y) \otimes s(X,Y)|^2 \quad (\text{S4})$$

in which we introduced the Fresnel function:

$$s(x,y) = -\frac{i}{\lambda z_0} \exp\left(\frac{i\pi}{\lambda z_0}(x^2+y^2)\right) \quad (\text{S5})$$

Its Fourier transform $S(u,v)$ is given by:

$$S(u,v) = -\frac{i}{\lambda z_0} \iint \exp\left(\frac{i\pi}{\lambda z_0}(x^2+y^2)\right) \exp(-2\pi i(xu+yv)) dx dy = \exp(-i\pi\lambda z_0(u^2+v^2))$$

(S6)

The hologram distribution in Eq.(S4) can be rewritten as:

$$H(X, Y) = \left| (1 + o(X, Y)) \otimes s(X, Y) \right|^2 \quad (\text{S7})$$

Taking into account that

$$1 \otimes s(X, Y) = -\frac{i}{\lambda z_0} \iint \exp\left(\frac{i\pi}{\lambda z_0} \left((x-X)^2 + (y-Y)^2\right)\right) dx dy = 1 \quad (\text{S8})$$

we expand the hologram distribution as:

$$H(X, Y) = 1 + o(X, Y) \otimes s(X, Y) + o^*(X, Y) \otimes s^*(X, Y) + |o(X, Y) \otimes s(X, Y)|^2 \quad (\text{S9})$$

Since we know from inline holography reconstruction that the first two terms represent the dominant information on the object, for further discussion we are neglecting the conjugate term and the small perturbation term:

$$H(X, Y) \approx 1 + o(X, Y) \otimes s(X, Y) \quad (\text{S10})$$

Reconstructing the hologram begins with calculating its Fourier transform:

$$\text{FT}[H(X, Y)] \approx \delta(u, v) + O(u, v) S(u, v) \quad (\text{S11})$$

It is then followed by multiplying with $S^*(u, v)$ and using $|S(u, v)|^2 = 1$:

$$S^*(u, v) \text{FT}[H(X, Y)] \approx S^*(u, v) \delta(u, v) + O(u, v) \quad (\text{S12})$$

Finally, the result is backward Fourier-transformed:

$$\text{FT}^{-1}\{S^*(u, v) \text{FT}[H(X, Y)]\} = 1 + o(x, y) \quad (\text{S13})$$

where we used:

$$\iint S^*(u, v) \delta(u, v) \exp(2\pi i(xu + yv)) dx dy = 1 \quad (\text{S14})$$

Therefore, according to Eq.(S13), the following equation applies:

$$S^*(u, v) \text{FT}[H(X, Y)] = \text{FT}[t(x, y)] \quad (\text{S15})$$

$FT[t(x,y)]$ is at the same time the wave scattered by the object and detected in the far-field in coherent diffraction imaging.

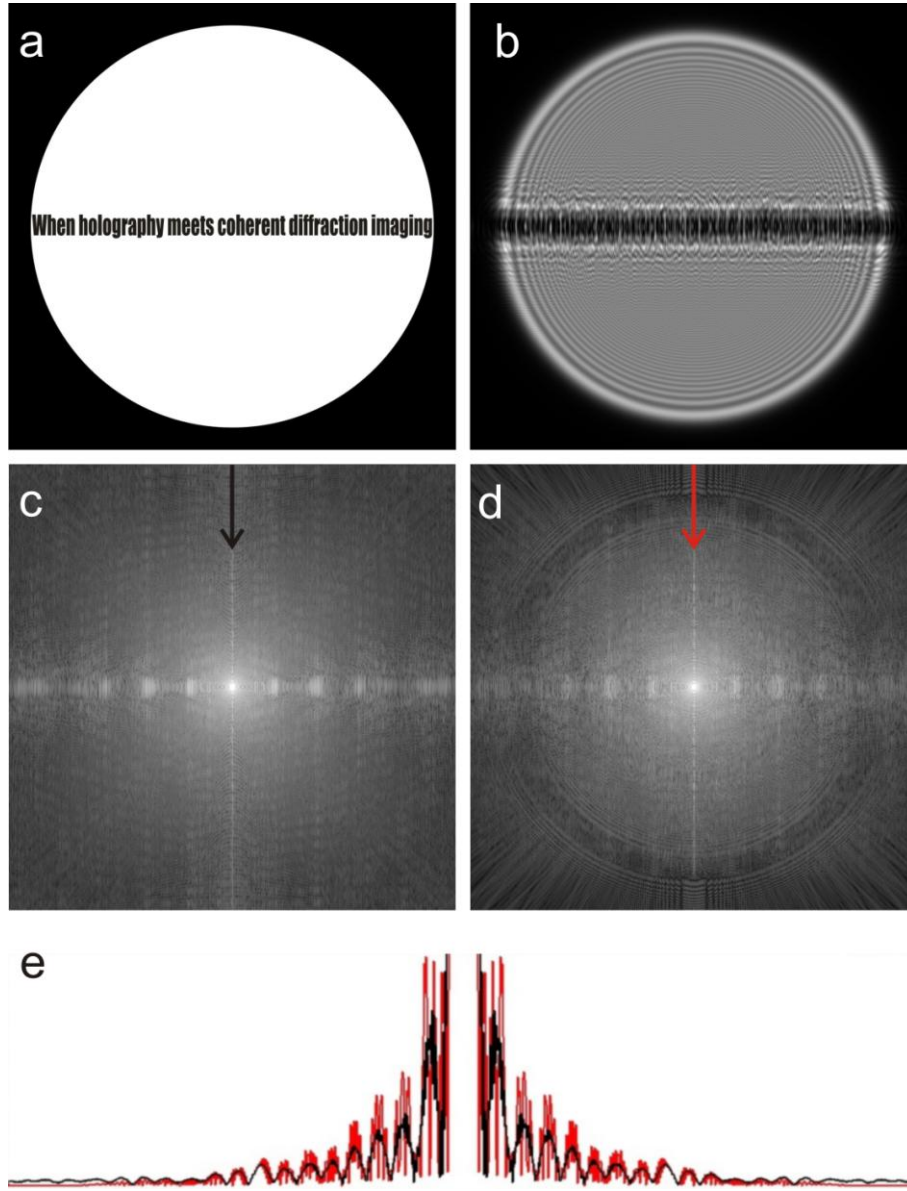
II. Simulated example

Here we support our HCDI method by a simulated example. The object, shown in Fig. S1a, is selected to be opaque and in the form of a line of text in order to challenge the resolution issue. The sample size amounts to $1.6 \times 1.6 \text{ mm}^2$ with the object placed over a hole in a nontransparent medium to mimic the experimental situation. The object is placed at 5.3 mm distance from the source. The wavelength is selected to be 532 nm and the hologram is recorded at 1 m distance on $30 \times 30 \text{ cm}^2$ screen sampled by 1000×1000 pixels as shown in Fig. S1b. The coherent diffraction pattern of the object at a distance of 905 mm behind the sample recorded on a $30 \times 30 \text{ cm}^2$ screen and sampled with 1000×1000 pixels is shown in Fig. S1c. The squared amplitude of the Fourier transform of the hologram is shown in Fig. S1d. The isomorphism between the diffraction pattern and the squared amplitude of the Fourier transform of the hologram is evident by comparing Fig. S1c with Fig. S1d and more precisely from the intensity profiles along the directions indicated by the arrows and displayed in Fig. S1e.

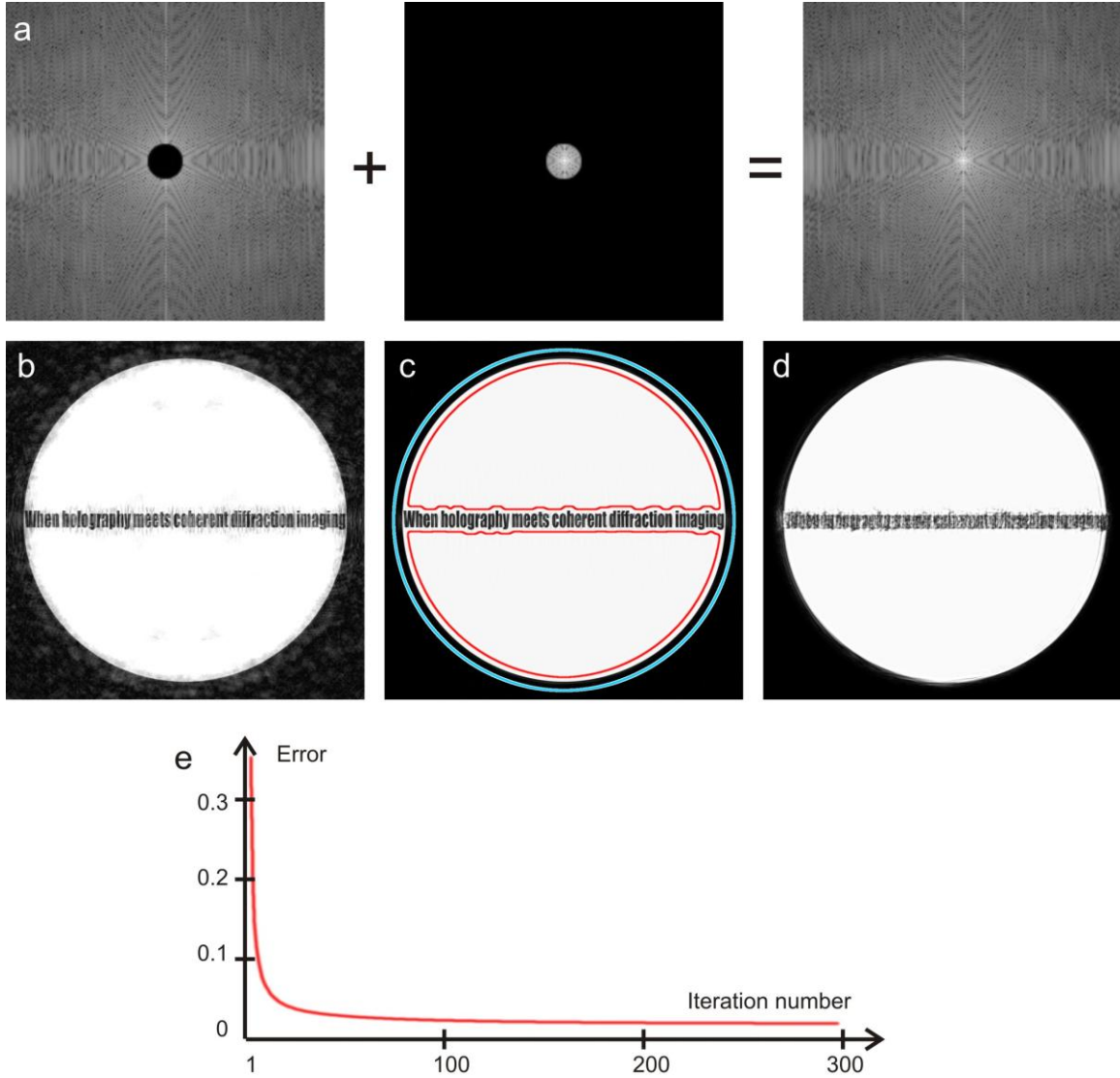
The simulated diffraction pattern is reconstructed by HCDI. For the 1st iteration, the central spot of diameter of 22 pixel in the diffraction pattern is replaced by the isomorphic central region of the squared amplitude of the Fourier transform of the hologram, as shown in Fig. S2a. For the remaining iterations the central spot is free from any constraints. The phase of the Fourier transform of the hologram is used at the 1st iteration only. The constraint in the object domain is purely based on the physics notion of non-negative absorption. The result of the reconstruction after 300 iterations is shown in Fig. S2b: the object text is almost perfectly recovered, though some artefacts remained. In another iterative run of the HCDI method, we additionally applied two loose support masks of about 20 pixels from the object contour. This leads to the elimination of the remaining artefacts in the reconstruction as evident from Fig. S2c. It is important to note that by employing a conventional reconstruction routine using the same constraints but a random initial phase distribution no meaningful convergence can be reached as illustrated in Fig. S2d. The reason is that at least in one direction, the horizontal one, the oversampling criterion is not fulfilled. The error function is calculated as:

$$\text{Error} = \frac{\sum ||U_0| - |U_i||}{\sum |U_0|}, \quad (\text{S16})$$

where $|U_0|$ is the square root of the measured intensity and $|U_i|$ is the updated amplitude of the complex wave at the detector plane after each iteration. The error function decreases rapidly with the number of iteration followed by an asymptotic approach towards zero, as displayed in Fig. S2e, and reaches 0.021 after 300 iterations.



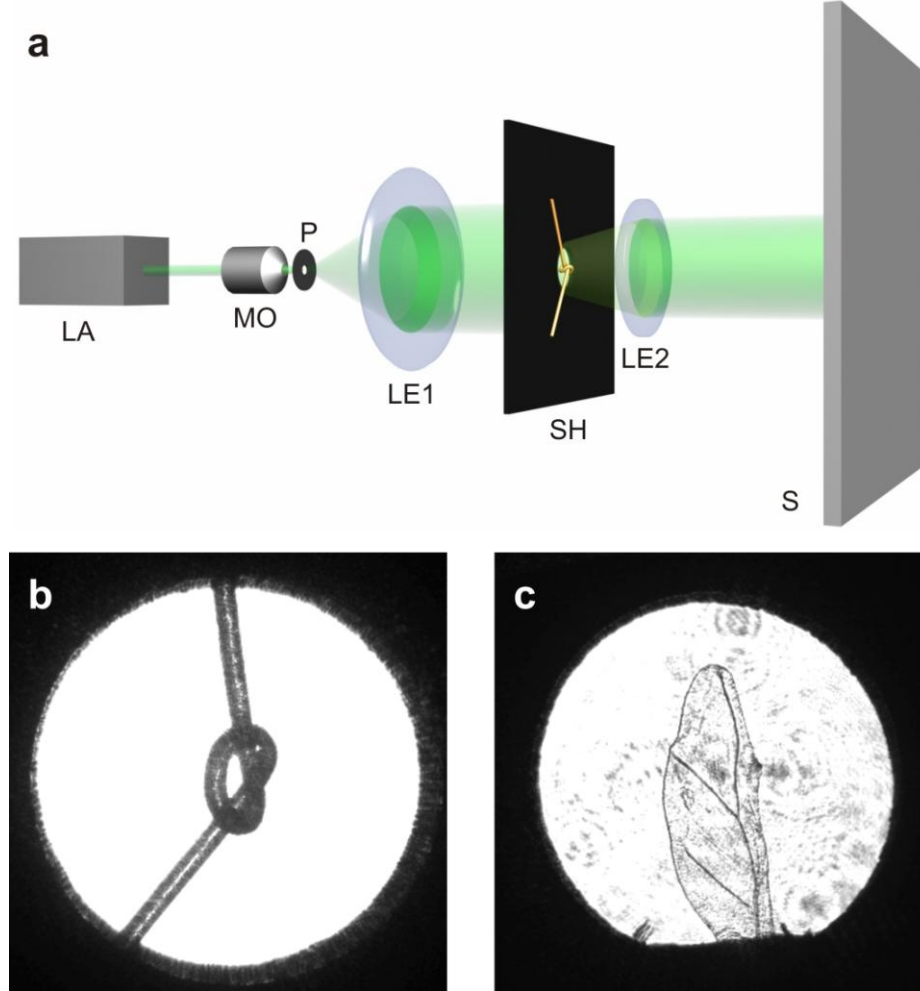
Supplementary FIG. S1 Simulated example of the HCDI method. **a**, Transmission function of the object. **b**, Hologram of the object. **c**, Diffraction pattern shown in logarithmic intensity scale. **d**, Squared amplitude of the Fourier transform of the hologram shown in logarithmic intensity scale. **e**, Intensity profiles along the directions indicated by the arrows in the diffraction pattern and the squared amplitude of the Fourier transform of the hologram.



Supplementary FIG. S2 Reconstruction by the HCDI method. **a**, The central region in the 1000x1000 pixel diffraction pattern is substituted by the central part of the squared amplitude of the Fourier transform. The central 200x200 pixel cut-outs are shown. **b**, Reconstruction using HCDI after 300 iterations employing a non-negative absorption filter. **c**, Reconstruction using HCDI after 300 iterations employing a non-negative absorption filter and two support masks, indicated in blue and red. **d**, Reconstruction after 300 iterations using a conventional CDI reconstruction routine starting with a random phase distribution, employing a non-negative absorption filter and the same support masks. **e**, Error as function of the iteration number for HCDI reconstruction in (c).

III. Experiments with objects imaged in transmission mode

After recording the diffraction patterns, a lens of $f=10$ mm was placed at about 10 mm behind the object and a transmission image of the objects with a magnification of about 90 was obtained on the screen, also shown in Fig. S3. The inner part of the hair appears as more transparent, in agreement with the reconstructions done by HCDI. Since a fly wing is very weakly absorbing, it constitutes mainly a phase object. This phase contrast apparent in the reconstruction done by HCDI is also verified by imaging in the transmission mode as displayed in Fig. S3b.



Supplementary FIG. S3 Optical transmission images of the objects. **a.** Schematic of the modified setup using an additional lens LE2. **b.** Hair. **c.** Fly wing. Since the fly wing constitutes a very weak absorbing object, the beam intensity had to be reduced. As a consequence, a disturbing background due to holographic images of out-of-focus dust particles on the lens surface became apparent.